CrossMark

Catastrophic Cooling in Superwinds: Line Emission and Non-equilibrium Ionization

William J. Gray[1,2], M. S. Oey[1] , Sergiy Silich[3] , and Evan Scannapieco[4]

[1] Department of Astronomy, University of Michigan, 1085 South University Ave., Ann Arbor, MI 48109, USA
[2] CLASP, College of Engineering, University of Michigan, 2455 Hayward St., Ann Arbor, MI 48109, USA
[3] Instituto Nacional de Astrofísica, Optica, y Electrónica, Puebla, AP 51, 72000 Puebla, Mexico
[4] School of Earth and Space Exploration, Arizona State University, USA

Abstract

Outflows are a pervasive feature of mechanical feedback from super star clusters (SSCs) in starburst galaxies, playing a fundamental role in galaxy evolution. Observations are now starting to confirm that outflows can undergo catastrophic cooling, suppressing adiabatic superwinds. Here we present a suite of one-dimensional, hydrodynamic simulations that study the ionization structure of these outflows and the resulting line emission generated by the cooling gas. We use the non-equilibrium atomic chemistry package within MAIHEM, our modified version of FLASH, which evolves the ionization state of the gas and computes the total cooling rate on an ion-by-ion basis. We find that catastrophically cooling models produce strong nebular line emission compared to adiabatic outflows. We also show that such models exhibit non-equilibrium conditions, thereby generating more highly ionized states than equivalent equilibrium models. When including photoionization from the parent SSC, catastrophically cooling models show strong C IV $\lambda1549$ and O VI $\lambda1037$ emission. For density-bounded photoionization, He II $\lambda1640$, $\lambda4686$, C III] $\lambda1908$, Si IV $\lambda1206$, and Si III $\lambda1400$ are also strongly enhanced. These lines are seen in extreme starbursts where catastrophic cooling is likely to occur, suggesting that they may serve as diagnostics of such conditions. The higher ionization generated by these flows may help to explain line emission that cannot be attributed to SSC photoionization alone.

Unified Astronomy Thesaurus concepts: Emission line galaxies (459); Starburst galaxies (1570); Interstellar plasma (851); Young massive clusters (2049); Stellar-interstellar interactions (1576)

1. Introduction

Outflows from galaxies and super star clusters (SSCs) are a pervasive feature of star-forming regions across all redshifts (Heckman et al. 1990, 2000, 2015; Lehnert & Heckman 1996; Pettini et al. 2002; Martin 2005; Rupke et al. 2005; Veilleux et al. 2005; Weiner et al. 2009; Bordoloi 2014; Rubin et al. 2014; Bordoloi et al. 2016; Chisholm et al. 2016). These outflows are powered by a variety of mechanisms including supernovae (Mac Low & Ferrara 1999; Scannapieco et al. 2001, 2002; Mori et al. 2002; Springel & Hernquist 2003; Dalla Vecchia & Schaye 2008; Creasey et al. 2013), stellar winds (Hopkins et al. 2012; Muratov et al. 2015; Hayward & Hopkins 2017), radiation pressure (Thompson et al. 2005; Hopkins et al. 2011; Murray et al. 2011), cosmic rays (Socrates et al. 2008; Uhlig et al. 2012; Farber et al. 2018), and hot gas produced by gravitationally driven motions (Sur et al. 2016). Outflows have a dramatic influence on their host galaxies, by slowing their chemical evolution (Tremonti et al. 2004; Oppenheimer et al. 2009; Davé et al. 2011; Agertz & Kravtsov 2015; Lu et al. 2015) and either suppressing star formation (Somerville & Primack 1999; Cole et al. 2000; Scannapieco et al. 2001, 2002; Benson et al. 2003) or enhancing star formation (Scannapieco et al. 2004; Gray & Scannapieco 2010, 2011a, 2011b; Bieri et al. 2016; Fragile et al. 2017; Mukherjee et al. 2018). Radiative and mechanical feedback from stellar clusters is a major driver of galaxy evolution and is especially important in the early universe, particularly during the epoch of reionization (e.g., Lehnert et al. 2010).

The nature of these outflows is complex, as the outflow gas is found over a wide range of temperatures. A complete picture is found only when observations and modeling encompass this full range, from X-ray observations of 10^7–10^8 K gas (Martin 1999; Strickland & Heckman 2007, 2009), near-UV and optical observations of $\approx10^4$ K (Pettini et al. 2001; Tremonti et al. 2007; Martin et al. 2012; Soto et al. 2012; Bik et al. 2018), and IR and submillimeter observations of molecular gas at 10–10^3 K (Walter et al. 2002; Sturm et al. 2011; Bolatto et al. 2013; Leroy et al. 2018). Most observational studies have focused on the near-UV and optical regime due to the strong rest-frame emission and absorption lines. X-ray observations, on the other hand, can be obtained only for the brightest nearby objects (Lehnert et al. 1999; Strickland & Heckman 2009).

The classic picture of stellar feedback from the parent stellar clusters is that of strong outflows that expel the residual gas, clear pathways for Lyman continuum (LyC) photons to escape their host galaxies (Heckman et al. 2011; Zastrow et al. 2013) and drive cosmic reionization (Faucher-Giguère et al. 2009; Lehnert et al. 2010; Bouwens et al. 2012). However, there is a growing body of evidence that the outflows are suppressed for the most massive and compact SSCs (Turner et al. 2003; Smith et al. 2006; Jaskot et al. 2017; Oey et al. 2017). This may be caused by very dense, overpressurized environments, or the outflows themselves, inducing catastrophic cooling (Wang 1995a; Silich et al. 2004; Krause & Diehl 2014; Silich & Tenorio-Tagle 2017, 2018; Yadav et al. 2017). The large pressure associated with such high densities, along with contributions from turbulence or gravitational sources, may also suppress these outflows through pressure confinement (e.g., Silich et al. 2007).

Several observations now seem to support this suppressed superwind scenario. Turner et al. (2003, 2017) studied an SSC still embedded in a molecular cloud in NGC 5253 and found

very narrow molecular line widths that imply velocities far lower than that expected for superwinds from a $10^5 \, M_\odot$ cluster. Cohen et al. (2018) also studied this cluster and found evidence that in this case the winds from the embedded massive stars may have stalled and a cluster-scale superwind is suppressed. Similar molecular kinematics are seen in Mrk 71, an SSC embedded in a dense, 2 pc H II region in NGC 2366 (Oey et al. 2017). Using optical spectroscopy of several SSCs in M82, Smith et al. (2006) found unusually high thermal and turbulent pressures that may have caused the incipient pressure-driven bubbles to stall (Silich et al. 2007), thereby preventing the launch of superwinds. Of particular interest, many of the so-called "Green Pea" galaxies show low outflow velocities and therefore may represent extreme starbursts with suppressed superwinds (Jaskot et al. 2017). These galaxies are excellent analogs of high-redshift galaxies due to their low metallicities, high UV luminosities, and large specific star formation rates (Cardamone et al. 2009; Izotov et al. 2011; Amorín et al. 2012).

If catastrophic cooling is responsible for suppressing superwinds from SSCs, then the strong radiation from such cooling may generate observable signatures of this process. Knowledge of the emitted line radiation can thus help distinguish between cooling versus pressure confinement as the dominant effect in this process. With this goal, we present some first-order calculations for a set of one-dimensional, spherically symmetric simulations that study the hydrodynamic, thermal, and ionization state of SSC outflows over a range of outflow velocities, and we present predictions for their line radiation.

We implement a wind boundary condition in the simulation domain that reproduces outflow properties at the star cluster surface (Chevalier & Clegg 1985; Cantó et al. 2000; Silich et al. 2004). The ionization state of the gas is evolved using a non-equilibrium atomic chemistry package that tracks the evolution of several astronomically important atomic ions and includes collisional ionization due to electrons, electron recombination, photoionization, photoheating, and ion-by-ion cooling.

The structure of the paper is as follows. An overview of galaxy outflows and possible cooling regimes is given in Section 2. Section 3 discusses the model framework and initial conditions along with the hydrodynamic results. The line emission is presented in Section 4, and the summary and conclusions are given in Section 5.

2. Outflow Structure and Cooling Regimes

The equations of mass, momentum, and energy conservation in the case of the steady-state outflows are

$$\frac{1}{r^2}\frac{d}{dr}(\rho u r^2) = q_m \tag{1}$$

$$\rho u \frac{du}{dr} = -\frac{dP}{dr} - q_m u \tag{2}$$

$$\frac{1}{r^2}\frac{d}{dr}\left[\rho u r^2\left(\frac{1}{2}u^2 + \frac{\gamma}{\gamma-1}\frac{P}{\rho}\right)\right] = q_e, \tag{3}$$

where r is the radial coordinate, ρ is the mass density, u is the velocity, P is the pressure, and γ is the adiabatic index. The mass and energy input rates are

$$q_m = \begin{cases} \dot{M}/V & \text{if } r \leqslant R_* \\ 0 & \text{if } r > R_* \end{cases} \tag{4}$$
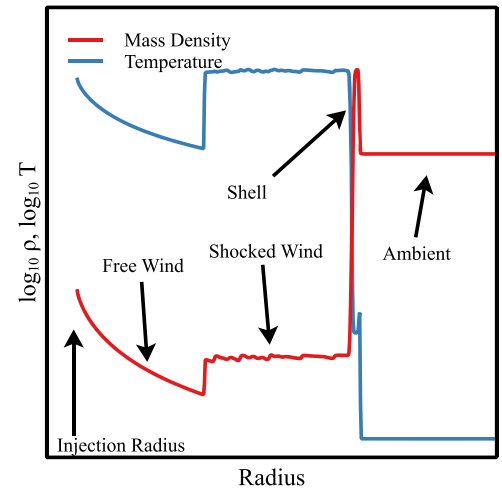

Figure 1. Schematic view of the outflow structure, highlighting hydrodynamically important regions. The red line represents the mass density, while the blue line represents the gas temperature. Labels give the four typical regions within the outflow, reproducing features described in Weaver et al. (1977).

$$q_e = \begin{cases} \dot{E}/V & \text{if } r \leqslant R_* \\ \sum_i -\Lambda_i n_i n_e & \text{if } r > R_* \end{cases} \tag{5}$$

where $\dot{M}$ and $\dot{E}$ are the mass and mechanical energy deposition rates within the cluster, R_* is the sonic radius, $V = 4\pi R_*^3/3$, n_i is the number density of species i, n_e is the electron number density, and Λ_i is the cooling function of species i. The classic outflow model of Chevalier & Clegg (1985), hereafter CC85, is recovered if one assumes that the outflow persists for many dynamical times and no heating or cooling occurs outside the sonic radius, (i.e., $q_e = 0$, or equivalently $\Lambda_i = 0$, for $r > R_*$).

Several authors have improved on this model by including heating and cooling within the outflow (e.g., Silich et al. 2004; Thompson et al. 2016), an incomplete conversion of stellar winds and SN mechanical energy into the outflow energy (heating efficiency; e.g., Stevens & Hartwell 2003; Silich et al. 2007, 2009; Wünsch et al. 2011), the presence of an ambient medium and radiation pressure effects (e.g., Krumholz & Matzner 2009; Martínez-González et al. 2014; Martin et al. 2015; Thompson et al. 2016; Rahner et al. 2017), the addition of a gravitational potential (e.g., Wang 1995a, 1995b; Bustard et al. 2016), and the effect of non-equilibrium heating and cooling on the ionization state of the outflow (Edgar & Chevalier 1986; Shapiro & Benjamin 1991; Gnat & Sternberg 2007; Kwak & Shelton 2010; Henley et al. 2012; Shelton & Kwak 2018; Gray et al. 2019). For a review of galactic outflows driven by stellar feedback see Zhang (2018).

The thermalization of stellar winds occurs at reverse shocks between neighboring massive stars in a cluster. For a $10^6 \, M_\odot$ SSC with 5 pc radius, the mean half-distance between its $\sim 10^4$ massive stars is $X \sim 0.2$ pc. It takes an extremely short time, a few hundred years ($\tau_{\rm therm} \sim X/v_{\rm inj}$, where the injection velocity $v_{\rm inj} \sim 1000 \, \text{km s}^{-1}$), to thermalize stellar winds. A slightly larger time, a few thousand years ($\tau_{\rm hom} \approx 1/3 R_{\rm inj}/v_{\rm inj}$) is required to fill in the star cluster volume with the gas reinserted by massive stars and form a homogeneous flow.

Figure 1 qualitatively shows the mass density, shown in red, and the temperature, shown in blue, of an outflow interacting with an ambient medium where cooling is not dynamically

important within the outflow. This figure reproduces the classic features found in Weaver et al. (1977), which are labeled in Figure 1. Four distinct regions are formed; the free-wind region, the shocked wind, the shock and forward shell, and the undisturbed ambient medium. The free-wind region begins at the sonic radius and is described by its density profile that follows the shape described in CC85. As the outflow interacts with the ambient medium, a reverse shock is generated that heats the free-wind region creating a zone of nearly uniform density and extreme temperatures. In front of this shocked region is a shell of swept-up gas from the ambient medium and the forward shock. Finally, beyond this shell is the undisturbed ambient medium.

The inclusion of radiative cooling can drastically modify both the temperature and density distribution within the outflow. Here we are interested in the cooling experienced in the free wind, shocked wind, and within the forward shell, and do not consider the flow structure inside the cluster. A series of models that aim to study the effect of cooling on the thermal and ionization structure of the outflow and its resulting line emission is presented.

3. Model Framework and Initial Conditions

All of the simulations presented here are performed using MAIHEM (Gray et al. 2015, 2019; Gray & Scannapieco 2016, 2017) our modified version of the adaptive mesh refinement hydrodynamics code FLASH (Fryxell et al. 2000). One of the primary components of MAIHEM is a non-equilibrium atomic chemistry and cooling package. This package tracks the evolution of 84 species across 13 atomic elements: hydrogen (H I–H II), helium (He I–He III), carbon (C I–C VII), nitrogen (N I–N VIII), oxygen (O I–O IX), neon (Ne I–Ne XI), sodium (Na I–Na VI), magnesium (Mg I–Mg VI), silicon (Si I–Si VI), sulfur (S I–S VI), argon (Ar I–Ar VI), calcium (Ca I–Ca VI), iron (Fe I–Fe VI), and electrons (e^-). For each species we consider collisional ionization by electrons, radiative and dielectronic recombinations, and charge-transfer reactions. Collisional ionization rates are taken from Voronov (1997), while radiative and dielectronic recombination rates are from a series of papers by Badnell and collaborators (Badnell et al. 2003; Badnell 2006). Coupled to this network is a cooling routine that computes the total cooling rate on an ion-by-ion basis. The procedure used in computing the cooling rates is the same as that presented in Gray et al. (2015) and is a reproduction of the results shown in Gnat & Ferland (2012). Examples of the instantaneous cooling rate from ETA006 (presented below), along with the atomic collisional ionization equilibrium (CIE) cooling rates, are given in Figure 2.

Radiation pressure from strong UV sources can affect the hydrodynamics and ionization state of the outflow. For example, it could enhance the gas thermal pressure behind the leading shock at the outer edge of the wind-driven shell (e.g., Martínez-González et al. 2014; Thompson et al. 2015). As presented in Gray et al. (2019), MAIHEM allows the UV background field to vary in space but is assumed to be static in time. This limitation prevents us from accurately including a UV background in our models and we therefore omit them. However, as presented below, we can approximate the effect of the UV field on the emission lines using a suite of CLOUDY models.
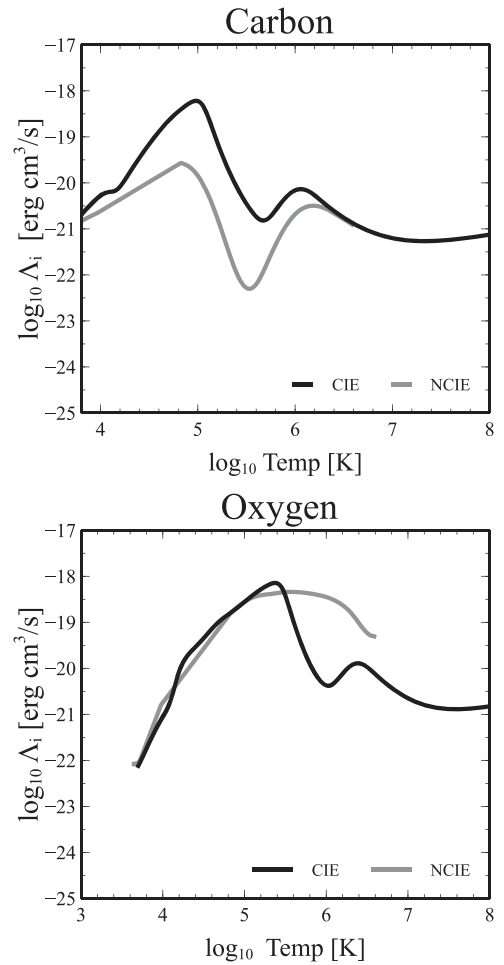

Figure 2. Top panel: ion-cooling functions for carbon. Bottom panel: ion-cooling functions for oxygen. The black line gives the CIE cooling curve, while the gray line shows the non-CIE cooling curve computed using results from ETA006 presented below. Note that for carbon the non-CIE rate is substantially lower than the CIE rate. Temperature is given along the x-axis, while the cooling rate is given along the y-axis.

3.1. Boundary Condition

Classically, the galaxy outflow is described by three parameters, the injection radius R_{inj}, mass-input rate $\dot{M}$, and the mechanical luminosity L_{mech}, of the enclosed cluster. We also consider two additional parameters, one that describes the density of the ambient medium, n_{amb} and one that describes the initial temperature of the ambient medium T_{amb}. The energy flux through the surface with radius R_{inj} is

$$\dot{E} = \eta L_{mech} = \eta \dot{M} (v_{inj}^2/2 + 3c_s^2/2), \qquad (6)$$

where c_s is the local sound speed and η is the heating efficiency, which determines how efficiently L_{mech} is converted to outflow energy (e.g., Wünsch et al. 2011). In our models, this is parameterized by varying v_{inj}. The outflow is implemented as an inflow boundary condition, following Gray et al. (2019).

Following CC85, we assume that the injection radius is coincident with the sonic radius and the injection velocity is therefore equal to the local sound speed (i.e., the gas enters the simulation domain with a Mach number of 1). The injection velocity is related to the enclosed cluster mechanical

Table 1
Simulation Summary

Name	$\dot{M}$ $(M_\odot \, \mathrm{yr}^{-1})$	R_{inj} (pc)	V_{inj} $(\mathrm{km \, s}^{-1})$	η	n_{amb} (cm^{-3})	T_{amb} (K)	ρ_{inj} $(10^{-24} \, \mathrm{gm/cm}^3)$	T_{inj} $(10^6 \, \mathrm{K})$
ETA100	10^{-2}	5	1000	1.00	500	10^2	8.4	72.6
ETA025	10^{-2}	5	500	0.25	500	10^2	16.8	18.1
ETA006	10^{-2}	5	250	0.06	500	10^2	33.6	4.5
ETA006N1	10^{-2}	5	250	0.06	1	10^4	33.6	4.5

Note. Summary of the simulations presented. The first column gives the name for each model. The second through seventh columns give the mass-input rate, injection radius, injection velocity, the heating efficiency, the injection mass density, and density and temperature of the ambient medium, respectively. The mass density and temperature at the injection (sonic) radius are given in columns 8 and 9.

luminosity as

$$c_s^2 = v_{\mathrm{inj}}^2 = \eta \dot{E} / 2\dot{M}. \qquad (7)$$

The mass density of the outflow is defined as

$$\rho_{\mathrm{inj}} = \dot{M} / \Omega \, R_{\mathrm{inj}}^2 v_{\mathrm{inj}}, \qquad (8)$$

or conversely,

$$\dot{M} = \Omega \, R_{\mathrm{inj}}^2 \rho_{\mathrm{inj}} v_{\mathrm{inj}}, \qquad (9)$$

where $\Omega R_{\mathrm{inj}}^2$ is the effective surface area of the outflow. For a perfectly isotropic outflow, $\Omega = 4\pi$. Here we take $\Omega = \pi$ following Gray et al. (2019) and Scannapieco (2017), based on the expectation that superwinds generally break out in preferred directions perpendicular to galaxy disks.

The initial ionization state of the outflow is determined by the initial temperature of the outflow and is given by

$$T_{\mathrm{inj}} = v_{\mathrm{inj}}^2 \bar{A} m_{\mathrm{H}} / k_{\mathrm{B}}, \qquad (10)$$

where m_{H} is the mass of hydrogen, $\bar{A}$ is the average atomic weight, and k_{B} is Boltzmann's constant. The atomic composition and total metallicity of the outflow is assumed to have a default solar value. Following Gray et al. (2019), we assume that the incoming gas is in CIE that depends only on the injection temperature, and when applicable, the UV field. The initial CIE values are computed using CLOUDY (e.g., Ferland et al. 2013). A table is generated that gives the CIE values as a function of temperature for each of the ionization states tracked by MAIHEM. This table is then read by MAIHEM at runtime and linearly interpolated to give the initial ionization state of the inflowing gas.

We caution that the flow parameterization from the sonic point in terms of $\dot{M}$ and $\eta\dot{E}$ is simplistic and is designed specifically to generate a range of outflow conditions, including catastrophic cooling. It is known that strong cooling and other effects also may be important inside the injection radius, which would further suppress the outflow (e.g., Wünsch et al. 2011; Silich & Tenorio-Tagle 2017). Therefore, the simulations presented here should be taken fairly qualitatively, as a demonstration of general effects.

3.2. Simulation Setup

Each simulation is run in one-dimensional, spherical coordinates with the inner radius equal to the injection radius R_{inj}, which is also defined to be the sonic radius and set to 5 pc by default; the outer radius is 75 pc. Initially, the entire domain

is considered to be part of the ambient medium. The initial density is set to n_{amb} with an initial temperature of 100 K with initial abundances in their CIE states. The base grid is comprised of 256 blocks and we allow up to two additional levels of refinement. The grid is allowed to adaptively refine based on gradients in the density, radial velocity, and gas temperature. This gives a maximum resolution of 0.14 pc. Each simulation is run for 1 Myr, which is much longer than the typical dynamical time of the outflow, $\tau_{\mathrm{dyn}} \approx R_{\mathrm{inj}}/v_{\mathrm{inj}}$.

As described above, there are five parameters that define each simulation: the injection (sonic) radius; the heating efficiency or, conversely, the injection velocity; the mass-input rate; and the density and initial temperature of the ambient medium. Table 1 gives a summary of the simulations presented here. We have chosen a small suite of models that fix the mass-input rate at $10^{-2} \, M_\odot \, \mathrm{yr}^{-1}$, the injection radius at 5 pc, and the outflow velocity at $1000 \, \mathrm{km \, s}^{-1}$. We vary the heating efficiency η between 1 and 0.06, which corresponds to equivalent injection velocities that range between 1000 and $250 \, \mathrm{km \, s}^{-1}$. We also assume an ambient medium that is initially neutral with a density of $500 \, \mathrm{cm}^{-3}$ and temperature of 100 K. We address the possibility of an ionized ambient medium in Section 4.2 below. Table 1 also gives the mass density and gas temperature at the injection (sonic) radius as computed by Equations (8) and (10), respectively. As we will show below, these parameters create conditions where cooling becomes hydrodynamically and chemically important in the outflow regimes introduced above.

3.3. Hydrodynamic Models

The mass density and temperature profile for each model are shown in Figure 3. The importance of the injection velocity is readily apparent in both panels. As shown in Table 1 and by Equation (8), the injection density is inversely proportional to the injection velocity, ranging between 8.4×10^{-24} and $33.6 \times 10^{-24} \, \mathrm{gm \, cm}^{-3}$ for the injection velocities considered. The temperature, however, is quadratically dependent on the injection velocity (Equation (10)) creating a much larger range of initial temperatures. As we will explore below, this change in initial temperature dramatically changes the initial ionization state of the inflowing gas.

ETA100 reproduces the density and temperature profiles found in Weaver et al. (1977) and CC85. This model shows prominent free-wind regions with profiles in density and temperature consistent with the adiabatic profiles found in CC85, which is shown by the black line in both panels of Figure 3 for comparison. This model also reproduces a notable
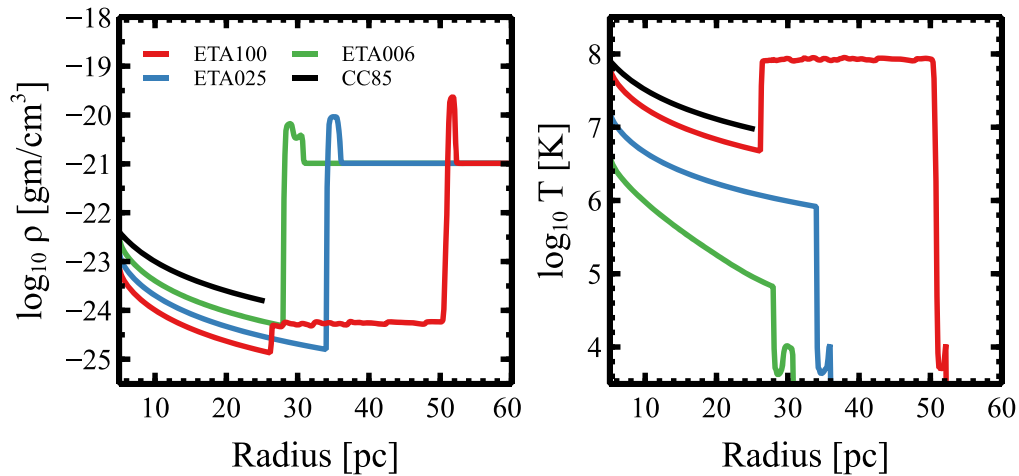
Figure 3. Left panel: logarithmic mass density. Right panel: logarithmic temperature profiles for each model at 1 Myr. The legend gives the line color for each model. The black line in each panel represents the density and temperature profiles expected from the Chevalier & Clegg (1985) adiabatic model solution.

shocked-wind region with nearly uniform densities and extremely high temperatures, $>10^8$ K.

ETA025, however, shows dramatic differences in both the density and temperature when compared to ETA100, and represents a regime in which cooling is important within the shocked-wind region. Specifically, Figure 3 shows that radiative cooling causes the shocked-wind region to collapse and it is completely absent in this model. This produces a density and temperature profile where only the free-wind and forward shock/shell regions are present. Note that the absence of the shocked-wind region allows the outflow to expand farther downwind compared to ETA100: the free-wind region extends to $R \approx 32$ pc for ETA025, while it only extends to ≈ 27 pc for ETA100. In this model, cooling within the free-wind region is dominated by the expansion of the outflow, since the temperature profile matches that found by assuming adiabatic expansion.

ETA006 represents a transition where cooling within the free wind itself is important. Figure 3 shows that when compared to ETA025, ETA006 is very similar in terms of the density structure and the absence of the shocked-wind region. ETA006, however, shows a steeper temperature profile within the free-wind region that indicates that atomic cooling is significant in this region. The low temperature within the forward shock in all three models is set by our cooling functions, which are only defined for $3.7 < \log T < 8$.

Figure 3 highlights the dramatic effect that simply changing the outflow conditions has on its resulting evolution. By changing the outflow velocity, the outflow can either produce the classic adiabatic evolution or undergo catastrophic cooling. The reason for this is twofold. First, the outflow density is slightly higher for the lower-velocity outflows, which increases the cooling efficiency since the cooling rate depends on n^2. This represents an increase in cooling efficiency of ≈ 16 between ETA100 and ETA006. Second, for solar metallicity gas, the cooling efficiency is higher at $T \approx 10^6$ K than at $T \approx 10^7$ K by roughly a factor of ten. This can be seen in the cooling curves of Sutherland & Dopita (1993) and Gnat & Ferland (2012). Together, this leads to a roughly a $160\times$ increase in the total cooling rate and the subsequent catastrophic cooling (e.g., Sutherland & Dopita 1993; Gnat & Sternberg 2007; Vasiliev 2011; Gnat 2017).

4. Line Emission

4.1. Ionization and Emission Due to Cooling

The strong cooling described in these models corresponds to radiation that may be characterized by its line emission. As shown above, the SSC outflows are found to have a wide range of temperatures. A complete picture is possible only when the properties of the outflow are measured and modeled over the full range of temperatures. Observational studies, however, often focus on the warm gas at $\approx 10^4$ K, where strong emission and absorption lines are found in the rest-frame UV and optical. This regime is also expected to dominate radiative cooling for strongly cooling flows (e.g., Gupta et al. 2016; Pellegrini et al. 2019). We have therefore selected a set of UV/optical emission lines to characterize each outflow. These are listed in Table 2.

The line emission for each of our simulations is estimated using CLOUDY. By default, CLOUDY assumes that the ionization state of the gas is in statistical and thermal equilibrium, which, as shown below and in Gray et al. (2019), may often not be met, especially in strongly cooling outflows. We therefore present two sets of CLOUDY line emission results, one in which the ionization states are in CIE, and one with non-equilibrium ionization states. To run the non-CIE case, the ionization states computed by MAIHEM are input into CLOUDY through the use of the "element name ionization" command, which freezes the ionization state distribution for a given element and requires CLOUDY to use this distribution when computing the line emission. It is therefore necessary to perform single-zone CLOUDY simulations for each of the ~ 500 radial steps in the MAIHEM model. In the CIE case, CLOUDY computes the ionization state of the gas. To optimize the comparison between these models, we use the same set of radial zones used in the non-CIE model to compute the ionization and emissivities.

Figures 4–6 show the calculated line emission as a function of radius for each of our models. The solid lines represent the line emissivities computed using the non-CIE, MAIHEM ionization states and the dotted line shows the equilibrium CLOUDY results. The legend in each panel shows the modeled emission lines. Appendix A shows similar figures but normalized by Hβ. Figure 7 shows a comparison between the fractional, non-CIE ionization states found in the MAIHEM models and the CIE ionization states computed by CLOUDY.
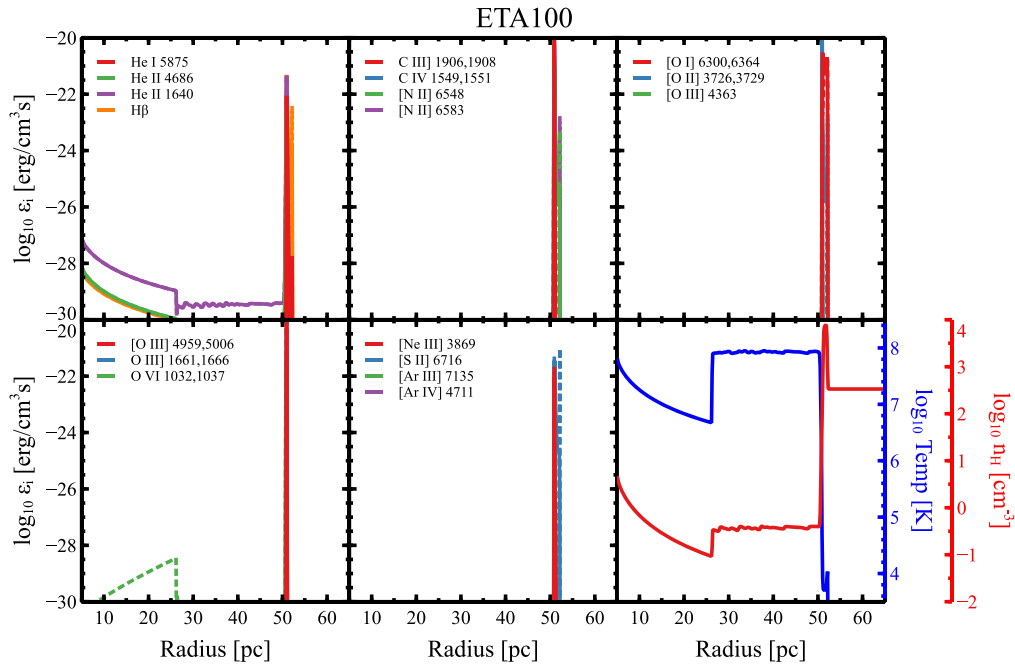
Figure 4. Line emission results for ETA100. The legend in each panel gives the emission lines plotted. The solid lines show the non-CIE MAIHEM results, while the dashed lines show CIE results from CLOUDY. Here, these results are nearly identical and are coincident with each other. The x-axis is the radial distance from the source of the outflow and the y-axis gives the logarithm of the line emissivity with units of erg cm^{-3} s^{-1}. The position of the forward shock is at 50 pc. The bottom right panel shows both the temperature density profiles. The blue line shows the temperature, while the red line shows the hydrogen number density.

Table 2
Line Luminosities Due to Hydrodynamics Only

Emission Line	ETA006-CIE	ETA006-nCIE
He I $\lambda 5875$	-3.35	-1.78
He II $\lambda 1640$	-1.41	-0.96
He II $\lambda 4686$	-2.73	-1.82
C III] $\lambda\lambda 1906,1908$	0.14	-1.37
C IV $\lambda 1549,1551$	0.59	-0.54
[N II] $\lambda 6548$	-1.04	0.31
[N II] $\lambda 6583$	-0.16	1.15
[O I] $\lambda\lambda 6300,6364$	2.13	1.49
[O II] $\lambda\lambda 3726,3729$	-0.55	0.76
[O III] $\lambda\lambda 1661,1666$	-0.29	-1.14
[O III] $\lambda 4363$	-1.14	-1.99
[O III] $\lambda\lambda 4959,5006$	-0.08	-0.91
O VI $\lambda\lambda 1032,1037$	0.84	0.29
[Ne III] $\lambda 3869$	-1.15	-1.61
Si III $\lambda\lambda 1393,1403$	-0.11	-1.09
Si IV $\lambda 1206$	-0.15	-1.50
[S II] $\lambda 6716$	1.14	0.83
[S II] $\lambda 6730$	0.98	0.68
[Ar III] $\lambda 7135$	-3.31	-2.02
[Ar IV] $\lambda 4711$	-2.40	-2.64
[Ar IV] $\lambda 4740$	-2.49	-2.72

Note. Emission-line luminosities for ETA006-CIE and ETA006-nCIE presented in Section 4.1. Line emission is given as $\log_{10} (\epsilon_i/\epsilon_{H\beta})$. The total H$\beta$ luminosity is 1.8×10^{36} erg s^{-1} and 3.3×10^{36} erg s^{-1} for ETA006-CIE and ETA006-nCIE, respectively. The first column gives the particular line, while the second and third columns give the results for ETA006-CIE and ETA006-nCIE, respectively. Note that emission-line luminosities from doublet lines (denoted with $\lambda\lambda$) are computed as the sum of the components.

In the case of ETA100, the MAIHEM, non-CIE, and CLOUDY, CIE results are essentially identical, which is shown in the left panel of Figure 7. As shown in Figure 3, this model has the

lowest outflow density and the highest outflow temperature. This creates a hot environment with very long recombination timescales, approximated as $\tau_{rec} = 1/\alpha n_e \sim 10^5 n_e^{-1}$ yr, where α is the recombination coefficient and n_e is the electron number density. Within the free-wind region, n_e is quite small, $\sim 10^{-1}$–1 cm^{-3}, leading to recombination timescales on the order of few $\times 10^5$–10^6 yr, which is long compared to the dynamical timescale $\tau_{dyn} \sim R_{shell}/v_{inj} \sim 5 \times 10^4$–$2 \times 10^5$ yr for the outflows considered here.

This model corresponds to the conventional, adiabatic bubble model, so the region interior to the shell is dominated by 10^7–10^8 K gas (Figure 3). Thus, the emission throughout the free-wind region and shocked-wind region is orders of magnitude fainter than the shell emission and generally is not observable. Only emission from He II and Hβ is present throughout the free-wind and shocked-wind regions. Both the He II and Hβ emission track the density profile for this model, reflecting these two distinct regions. Only in the high-density shell at the forward shock do the other nebular emission lines become apparent, creating very sharp emission features in, e.g., [C III] and [O III].

Figure 5 and the middle panel of Figure 7 show the results for ETA025. Similar to ETA100, He II, and Hβ emission, along with emission from O VI, dominates throughout the free-wind region and all other emission lines appear only at the high-density shell. Compared to ETA100, the He II emission in ETA025 shows only a single, continuous profile corresponding to only the free-wind region, again reflecting its density profile. While otherwise similar to ETA100, the emissivity of He II and Hβ is at least an order of magnitude greater in this region, and may be easier to detect. Although difficult to see in emission, ETA025 shows some differences between the equilibrium and non-equilibrium chemistry and associated line emission. For example, C IV $\lambda 1549$, 1551, [C III] $\lambda 1906$, and C III] $\lambda 1908$, are
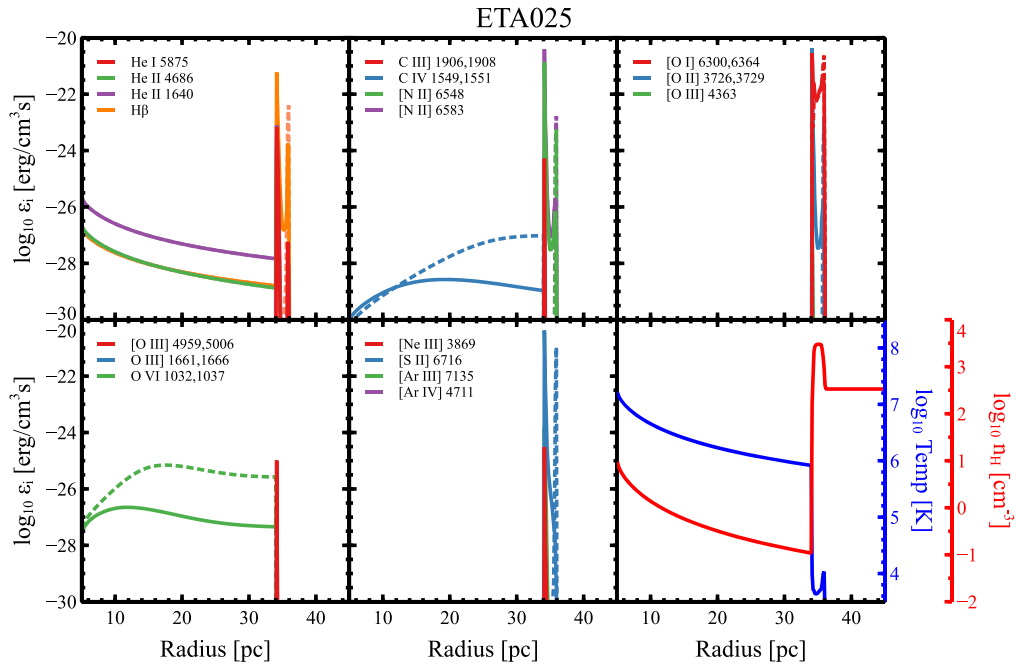
Figure 5. Same as Figure 4 for model ETA025. In many cases, the equilibrium and non-equilibrium results are coincident. The final position of the forward shock is found at 37 pc.
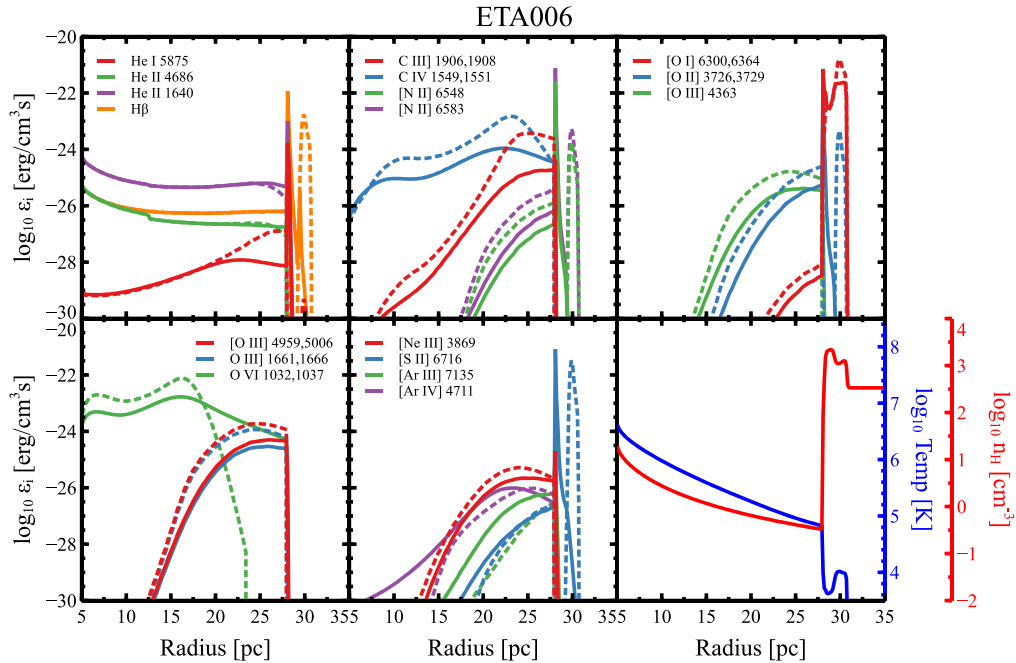

Figure 6. Same as Figure 4 for model ETA006. The final position of the forward shock is found at 28 pc.

up to two orders of magnitude weaker in the non-equilibrium models compared to the equilibrium results.

Figure 6 shows the results for ETA006. In addition to being the most interesting model hydrodynamically, it is the coolest model and therefore has the strongest nebular line emission. Nearly every emission line that we compute is strongly emitting throughout the free-wind region. The line profiles have similar shapes, generally increasing with radius in the outflow and peaking at or near the shell, except for the highest ionization states of oxygen. The strong emission in this model is due to the density and temperature of the outflow, and

roughly traces the gas at $T \sim 10^5$ K. The lower outflow temperatures and higher electron densities lead to lower recombination timescales. This allows the outflow gas to recombine into lower ionization states, increasing the abundances of those ions under consideration.

The right panel of Figure 7 shows the ionization state comparison between MAIHEM and CLOUDY for ETA006. While the non-equilibrium and equilibrium models agree to within roughly an order of magnitude for most ionization states, significant differences are seen. The CIE model tends to favor lower ionization states for the selected ions and an
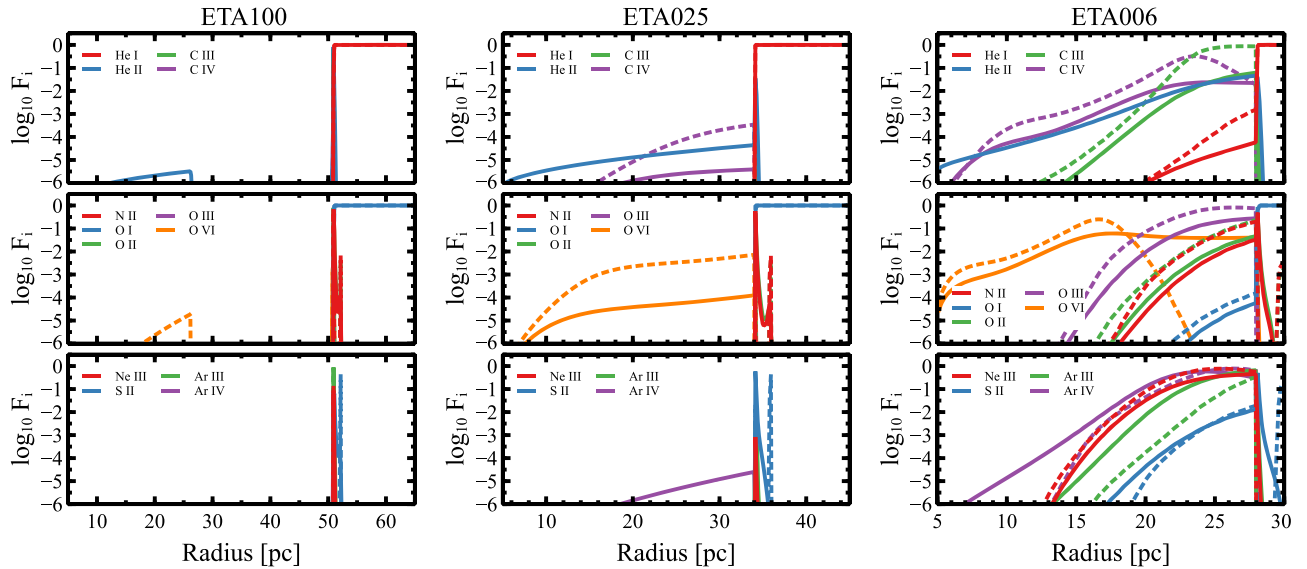
Figure 7. Fractional ionization comparisons as a function of radius for ETA100 (left panel), ETA025 (middle panel), and ETA006 (right panel). The legend in each panel describes the ions. The solid lines show the non-equilibrium results from the MAIHEM models, while the dashed lines are equilibrium results computed using CLOUDY. Note that CIE conditions tend to predict outflows with lower ionization states compared to the non-CIE outflows.

outflow with more neutral gas. Similarly, the CIE model slightly overpredicts the line emission compared to the non-equilibrium model.

Overall, Figures 4–7 highlight the importance of following the non-equilibrium atomic chemistry in these systems. Except for ETA100, which has the lowest outflow density and highest outflow temperature, every model produces ionization states that are out of thermal equilibrium. In general, the non-equilibrium models produce a more ionized medium. This directly impacts the line emission produced, such that the CIE models produce stronger emission for several lines. For example, C IV λ1549 and C IV λ1551 are overproduced in both ETA025 and ETA006, while [O III] λ5006 and [O III] λ4363 are overproduced in ETA006.

Table 2 gives the integrated line luminosities from the CIE and non-CIE models for ETA006. The integrated line luminosity is given by

$$L_i = 4\pi \int_{R_{\rm inj}}^{R_{\rm H\,II}} \epsilon_i r^2 dr, \qquad (11)$$

where r is radial distance and ϵ_i is the volume emissivity of line i. We integrate over the outflow region from the injection radius up to the boundary of the ionized region, at the shell. The simulations in this section do not include "precursor" photoionization outside the shell due to the generated radiation (e.g., Shull 1979), but this photoionized intensity is small relative to the shell emission.

4.2. Contribution of Photoionization

We now aim to estimate the effect of photoionization on the line emission from these outflow models. In particular, we evaluate the effect of photoionization using the temperature and density profiles generated by MAIHEM. As mentioned above, strong radiation can have important effects on the hydrodynamics of the outflow. However, these effects are absent in our MAIHEM models, as they are unable to carry out the

Table 3
Summary of Photoionization Models

Name	MAIHEM Density	MAIHEM Temperature	SB99 UV Field
ETA006-A	✓	✓	
ETA006-B	✓		✓
ETA006-C	✓	✓	✓
ETA006N1	✓	✓	✓

Note. Summary of the photoionized models presented. ETA006-A, ETA006-B, and ETA006-C use density and temperature profiles from ETA006. ETA006N1 uses density and temperature profiles taken from a model like ETA006, but with an ambient medium set to 1 cm^{-3}.

frequency-dependent radiative transfer calculation necessary to handle them properly.

We note that the wind-driven shell never expands beyond the photoionized region in any of the models with the high ambient density (e.g., Dove et al. 2000), which we examine in Section 4.1. In the ETA100 case, the central cluster photoionizes only a small mass fraction of the swept-up shell ($M_{\rm H\,II}/M_{\rm sh} \sim 0.03$), whereas in models ETA025 and ETA006 the ionized gas fraction increases due to smaller wind-driven shell radii and ionized gas densities that drop with $v_{\rm inj}$: $M_{\rm H\,II}/M_{\rm sh} \sim 0.3$ and $M_{\rm H\,II}/M_{\rm sh} \sim 0.75$ in models ETA025 and ETA006, respectively (see Appendix B). Nevertheless, in all cases LyC photons are trapped within the wind-driven shell. Note also that photoionization makes the shells thicker, since in the photoionized region the gas temperature is ~2.5 times larger than the minimum values obtained in our calculations, resulting in ~2.5 times smaller gas density than the maximum values (see Figure 3).

To estimate the effect of photoionization on the line emission, we post-process the MAIHEM results using CLOUDY, now including photoionization from a radiation field representing that of the parent SSC. In the previous Section 4.1, the line emission was independently modeled at the individual radial steps, which was necessary to estimate the line emission using the non-equilibrium ionization states produced by MAIHEM.
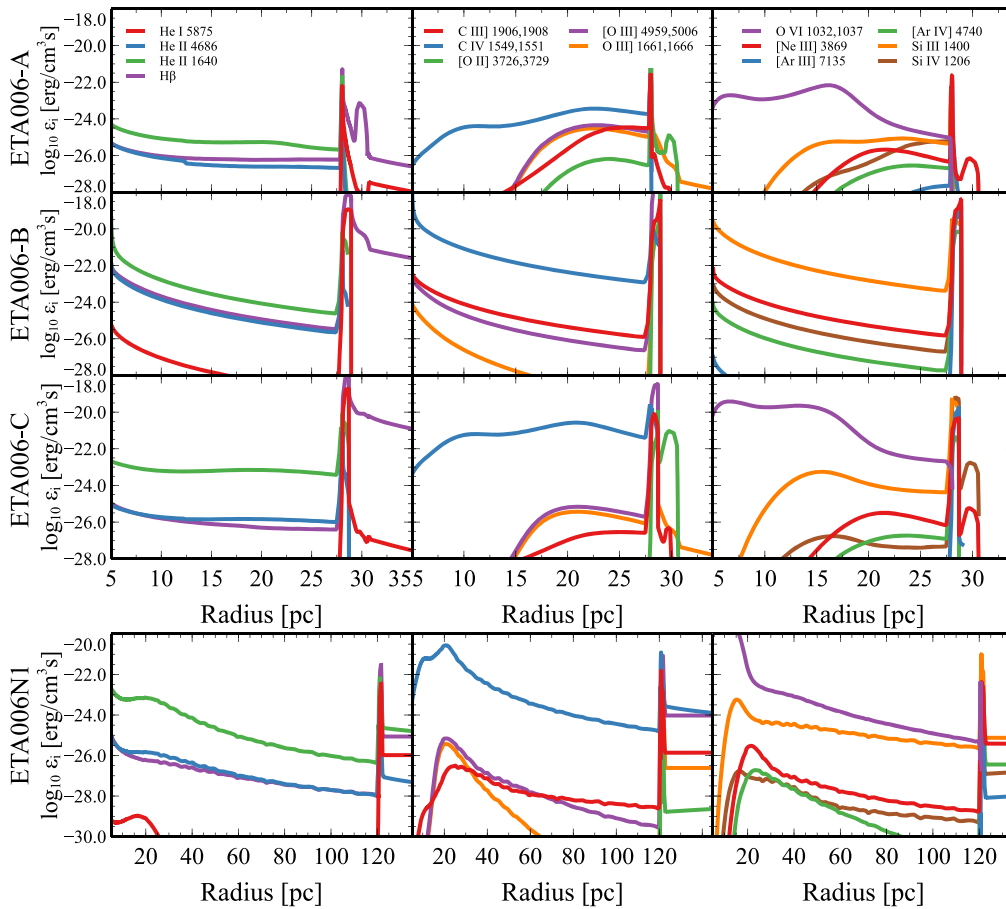
Gray et al.

Figure 8. CLOUDY line emission comparison for ETA006 models. Each column shows a set of emission lines as described by the legend in the first row. The first row shows MAIHEM density and temperature profiles without photoionization (ETA006-A); the second shows the MAIHEM density profile only with photoionization (ETA006-B); the third shows MAIHEM density and temperature profiles with photoionization (ETA006-C); and the last row shows the same model based on ETA006 but with an initial ambient temperature of 10^4 K and density of 1 cm^{-3} (ETA006N1). The ionized region extends to 2500 pc for ETA006N1. Note that the x-axis scale for this model is much larger than for the others.

Therefore, the line emission for both the CIE and non-CIE models were calculated piecemeal. However, in this section, modeling the photoionization requires a single, multi-zone CLOUDY model in order to properly propagate the photoionization outward from R_{inj}. This also requires that the ionization states be in equilibrium given the imposed radiation field. Therefore, in this section, only the radial density and/or temperature profiles from MAIHEM are taken as input, and not the non-equilibrium ionic abundances shown in the previous section. The variation between equilibrium and non-equilibrium emission for the photoionized cases can be qualitatively evaluated based on results from Section 4.1.

We employ Starburst99 (SB99; Leitherer et al. 1999) to generate the ionizing spectral energy distribution. The SB99 model is run with fixed stellar mass of 4.1×10^6 $M_\odot$, solar metallicity, a Salpeter initial mass function, and an age of 1 Myr, consistent with the final age of the MAIHEM simulations. This combination of parameters gives a model with a mass loss rate of 10^{-2} $M_\odot$ yr^{-1} and a total luminosity of 10^{43} erg s^{-1}, matching the mass-input rate of the MAIHEM models.

As shown above, models ETA100 and ETA025 have temperatures and ionization states that are too high to produce nebular collisional line emission within the free-wind region and hot shocked-wind region. Thus, the inclusion of photoionization also has no effect on the resulting line emission for these species. On the other hand, ETA006, with its higher densities, lower temperatures, and lower average ionization states, does produce a variety of line emission throughout the free-wind region. Therefore, we focus on ETA006 to examine how photoionization affects its line emission.

We compare four variations of this model as follows:

1. ETA006-A: the hydrodynamic case with no photoionization, but density and temperature profiles taken from MAIHEM. This model is similar to the CIE model as presented in Section 4.1. We discuss the differences between these models below.
2. ETA006-B: a model that includes photoionization, adopting only the density profile from MAIHEM, and not the temperature profile. All species are assumed initially neutral and any changes in ionization state are solely due to the UV source. This model represents the pure photoionization limit.
3. ETA006-C: a photoionization model using both density and temperature profiles taken from the MAIHEM model.
4. ETA006N1: the same as ETA006-C but for a model with an initial ambient temperature of 10^4 K and ambient density of 1 cm^{-3}.

These models are summarized in Table 3.

Figure 8 shows the line emissivities for each of these models in rows 1–4, respectively. We have chosen to plot a subset of

Table 4
Line Luminosities Including Photoionization

Emission Line	ETA006-A	ETA006-B	ETA006-C	ETA006N1-$R_{\rm shell}$	ETA006N1-$R_{\rm H\,II}$
He I $\lambda5875$	−1.00	−0.82	−0.80	−1.00	−0.91
He II $\lambda1640$	−0.30	−2.54	−2.45	−0.60	−2.41
He II $\lambda4686$	−1.19	−4.07	−4.01	−1.82	−4.06
C III] $\lambda\lambda1906,1908$	−0.04	−0.95	−2.20	−0.50	−0.58
C IV $\lambda\lambda1549,1551$	−0.13	−2.07	−1.42	0.77	−1.21
[N II] $\lambda6548$	0.07	−1.63	−1.71	−3.50	−1.37
[N II] $\lambda6583$	1.07	−0.80	−2.32	−2.35	−0.39
[O I] $\lambda\lambda6300,6364$	1.46	−2.37	−1.38	−7.90	−3.13
[O II] $\lambda\lambda3726,3729$	0.69	−1.01	−2.64	−2.74	−0.78
[O III] $\lambda\lambda1661,1666$	−0.80	−1.94	−3.67	−0.87	−1.51
[O III] $\lambda4363$	−1.38	−1.75	−3.50	−1.45	−1.40
[O III] $\lambda\lambda4959,5006$	0.29	0.88	−0.52	0.68	1.07
O VI $\lambda\lambda1032,1037$	0.39	−9.30	−1.39	0.72	−1.55
[Ne III] $\lambda3869$	−0.24	−0.61	−2.34	−0.71	−0.37
Si IV $\lambda1206$	−1.36	−1.30	−1.37	0.36	−1.24
Si III $\lambda\lambda1393,1403$	−0.73	−1.09	−1.17	0.09	−1.12
[S II] $\lambda6716$	1.62	−1.78	−1.19	−3.82	−1.34
[S II] $\lambda6730$	1.46	−1.64	−1.32	−3.96	−1.51
[Ar III] $\lambda7135$	−0.70	−1.00	−1.99	−1.81	−0.85
[Ar IV] $\lambda4711$	−2.84	−1.88	−3.25	−1.62	−1.66
[Ar IV] $\lambda4740$	−2.94	−2.02	−3.38	−1.76	−1.81

Note. Line luminosity for CLOUDY models presented in Section 4.2. Line emission is given as $\log_{10} (\epsilon_i/\epsilon_{\rm H\beta})$. ETA006-A has a total H$\beta$ luminosity 5.4×10^{36} erg s^{-1}, ETA006-B of 9.5×10^{40} erg s^{-1}, and ETA006-C of 9.5×10^{40} erg s^{-1}. Two sets of results are shown for ETA006N1: column 5 shows the results where we integrate up through the forward shell and column 6 where we integrate up through the entire H II region. The total Hβ luminosity is 7.8×10^{38} erg s^{-1} and 1.5×10^{41} erg s^{-1} for each case, respectively. Note that emission-line luminosities from doublet lines (denoted with $\lambda\lambda$) are computed as the sum of the components.

emission lines in order to simplify the presentation. A version of Figure 8 but with each line normalized by Hβ is given in Appendix A. Table 4 presents the integrated line luminosities for these models, calculated as before. For all models except ETA006N1, the ionized boundary is coincident with the forward shell since the shell is optically thick to LyC photons, as noted above. For ETA006N1, the shell is optically thin. Column 5 of Table 4 gives the luminosities integrated only within the shell outer radius, while column 6 gives values integrated through the entire H II region, which extends to a radius of ∼2500 pc.

Model ETA006-A represents the model for emission due only to the hydrodynamics. It is the same as the CIE model presented in Section 4.1, but as noted above, it is run as a single CLOUDY model. The photoionizing radiation field that CLOUDY propagates is comprised of two components, an incident field defined by the user, and a diffuse field that is generated by hot gas within the CLOUDY model. For ETA006-A, the user-defined field is not included, and therefore it is the diffuse field that generates the minor differences between single-zone (Figure 8) and multi-zone (Figure 6) emissivities. In particular, we see that the ambient medium is now photoionized, as seen in precursor H II regions for shock emission (e.g., Shull 1979). The effect of shock expansion into an ionized medium is explored with other models below.

Model ETA006-B is the limiting model for pure photoionization, which we include to show the effects of only photoionization and photoheating (upper left panel of Figure 9). Whereas the ionization states for model ETA006-A are set by shock-heated temperatures that are 1–2 orders of magnitude greater, the ionization structure of ETA006-B is largely uniform with radius, with the gas dominated by C IV $\lambda1551$ up to the high-density shell (Figure 8). As noted in the

previous section, the line emissivities in catastrophically cooling outflows differ markedly from their density profiles due to the temperature distribution of 10^5 K gas. Therefore, the ionization structure of ETA006-B is very different from ETA006-A, as shown for carbon in the upper right panel of Figure 9 (see also the right panel of Figure 7).

Model ETA006-C combines both the hydrodynamic heating and SSC photoionization. Comparing ETA006-A and ETA006-C elucidates the contribution of fluorescence and photoionization to the line emission, demonstrating that these significantly boost the line emission of some species. For example, C IV $\lambda1549,1551$ and O VI $\lambda1037$ are enhanced by over two orders of magnitude within the free-wind region, largely at the expense of C III] and [O III] (Figure 8). This is true even though the abundance of C IV and the gas temperatures are essentially the same between the two models (Figure 9, top right panel).

The integrated line luminosities, however, are dominated by the high-density shell (Table 4). Because the photoionizing radiation is diluted at the large shell radius and the shell gas density is high, the ionization parameter in the shell is low, resulting in weak [O III] and [Ar IV]. Nevertheless, the strong C IV and O VI emission generated by the strongly cooling wind (e.g., Model ETA006-A) maintains line strengths in these ions well above nebular photoionized values. This suggests that these lines may offer important diagnostics of catastrophically cooling outflows.

A weak, cooling outflow likely expands into an ambient medium that is already photoionized by the SSC. We approximate this condition by also running the MAIHEM model for ETA006 but set an ambient medium temperature of 10^4 K instead of 10^2 K. Given the high ambient density of 500 cm^{-3}, this model strongly recombines, thus we find no significant
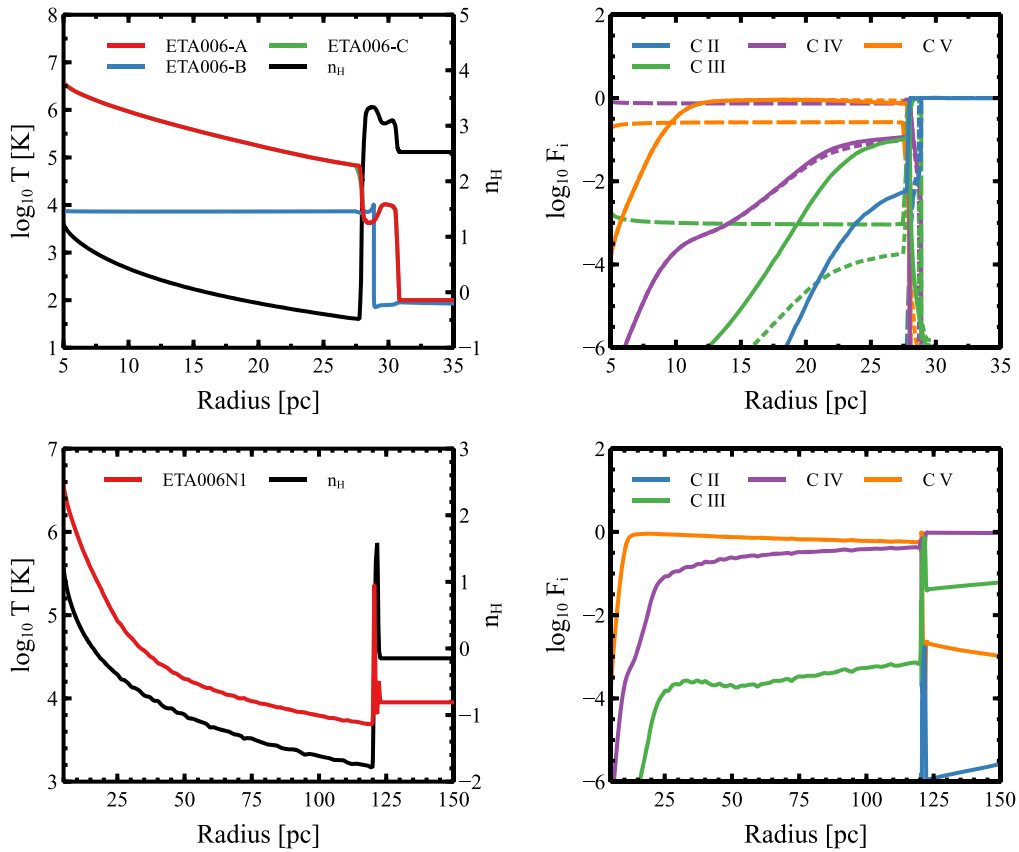
Figure 9. Top left panel: temperature profiles used as input into the CLOUDY photoionization models for ETA006 variations. The solid black line shows the hydrogen number density and is common to each model. Note that ETA006-A and ETA006-C have nearly identical ionization states and therefore are indistinguishable in the figure. Top right panel: final ionization states for carbon as a function of radius for ETA006-A (solid lines), ETA006-B (dashed lines), and ETA006-C (dotted lines). Generally, ETA006-A and ETA006-C again are nearly indistinguishable. Bottom left panel: temperature and density profiles used for ETA006N1. Bottom right panel: final ionization for carbon for ETA006N1C is shown for comparison.

difference in line emissivities between this model and ETA006-C.

Since more realistic ambient densities will strongly decrease as a function of radius from the SSC, we also consider another model, ETA006N1, where the ambient density is lowered to $1\,\mathrm{cm}^{-3}$ and the ambient temperature is set to $10^4\,\mathrm{K}$, but is otherwise identical to ETA006. We have post-processed ETA006N1 in the same manner as ETA006-C, that is, with the density and temperature profiles generated by ETA006N1 and with the SB99 UV field.

The results for this model are shown as the fourth row in Figure 8. This model is more closely related to ETA025 (Section 4.1), as seen in the temperature and density profile for ETA006N1 shown in the bottom row of Figure 9. Unsurprisingly, the outflow expands much farther in ETA006N1 owing to the lower ambient density. We also see that the ionization structure now more closely resembles that of the pure photoionization model ETA006-B, particularly at large radii, where the line emissivities generally decrease with radius in the free-wind region. The most prominent difference between ETA006N1 and ETA006-B is strong O VI emission throughout, and the enhanced C IV emission at small radii. There is also a central gap in emission for most species. ETA006N1 also continues the trend of large C IV/C III ratios throughout the free-wind region.

However, in particular, we see that the ambient medium is fully photoionized by the SSC in this model. The photoionization extends to a radius of 2500 pc, so the dense shell would

likely appear as a density-bounded H II region. In contrast, for ETA006-B, the only low-level photoionization outside the shell is due to the precursor radiation described above. Similarly, we showed earlier that ETA025 would have an optically thick shell if photoionized by the SSC.

As noted above, column 5 of Table 4 provides total line luminosities for this model integrated only through the outer boundary of the shell; these simulate observations of only the density-bounded, shell H II region, corresponding to spatially resolved observations or data that is dominated by the high surface-brightness emission. We see that density-bounded conditions strongly affect emission in He II, C III], Si IV, and Si III, which are all greatly enhanced. Column 6 gives line emission integrated through the total, 2500 pc H II region. While the integrated nebular emission differs significantly depending on the limiting radius, we see that for both tabulated cases, the C IV and O VI emission remain significantly elevated above the pure photoionized values of ETA006-B.

5. Discussion

5.1. Optical Depth and LyC Escape

We find that in our one-dimensional simulations, the swept-up shell is optically thick to the radiation from the SSC for the default parameters in model ETA006 (see Dove et al. 2000, Appendix B). This prevents the cluster radiation from penetrating into the undisturbed ambient medium, which is at odds with observations linking such systems to Green Peas and

other LyC emitters (Jaskot & Oey 2013; Jaskot et al. 2017). However, this optical thickness is most likely due to the constrained geometry of 1D simulations, which does not allow for the possibility of the shell breaking up into clumps. Clumping would naturally lead to increased leakage of LyC photons (Jaskot et al. 2019). In multidimensional simulations, the shell is likely to be susceptible to the Rayleigh–Taylor instability (Rayleigh 1883; Taylor 1950), which can break up the shell into clumps on the order of the shell thickness. Moreover, catastrophic cooling conditions should also strongly induce the cooling instability, which can increase density perturbations by over an order of magnitude (Scannapieco 2017). Thermal instability can cause clumping in the free wind itself (e.g., Thompson et al. 2016; Schneider et al. 2018), or even at radii $<R_{inj}$, thereby decreasing the initial heating efficiency (Wünsch et al. 2011). However, even when these additional hydrodynamic effects are taken into account, it is possible to generate lines of sight without clumps, or lines of sight with average densities similar to those modeled here. In this case, we expect the results from these one-dimensional simulations to model these lines of sight.

Evidence does suggest that extreme Green Peas are strongly clumped, consistent with this catastrophic cooling scenario. A number of studies point to a "picket fence" geometry in these and similar candidate LyC emitters, noted from absorption-line and neutral gas studies (e.g., Heckman et al. 2011; Rivera-Thorsen et al. 2017; McKinney et al. 2019). Jaskot et al. (2019) show that the SSC environment in extreme Green Peas is consistent with a two-component model consisting of optically thick, high-density clumps at close quarters to the SSCs, which generate the extreme ionization parameters; and an optically thin, interclump medium, through which LyC radiation can escape.

In addition, we do find in some simulations that if the shell expands into a lower-density ambient medium, it becomes possible to form an optically thin shell (e.g., ETA006N1; Figure 8). Thus, the optical depths in the simulations presented in this work are not incompatible with suppressed superwinds being linked to LyC emitters. Future studies will examine these issues using a wider range of outflow parameters.

5.2. Line Diagnostics of Catastrophic Cooling

Our models predict that catastrophically cooling winds generate strong C IV and O VI emission that is not observed in ordinary, photoionized H II regions. C III] is strongly elevated in models for cooling outflows expanding into low-density ambient medium, but greatly suppressed when the ambient density is high. Interestingly, emission in all these lines appears to be linked to the most intense starbursts. Strong, nebular C IV, C III], and He II $\lambda1640$ have been reported in, e.g., nearby ($z \lesssim 0.2$) high-excitation, compact dwarf starbursts identified by Senchyna et al. (2017) and Berg et al. (2019b) from SDSS; and also in $z \sim 3$, luminous Lyα emitters selected by Amorín et al. (2017) to have strong C III] and O III].

Hayes et al. (2016) present imaging in O VI $\lambda1037$ of an extreme, nearby starburst, J1156+5008. While the scale of this starburst and resultant emission is much larger than our models, the qualitative features may be consistent with our predictions. There is a clear, 9 kpc shell around the starburst. In one analysis, a central, 1 kpc region centered on the starburst also shows positive emission. However, the authors suggest that this apparent emission is spurious, based on their lack of confidence

in the continuum-subtraction method. We note, however, that our models do predict strong central O VI emission, in addition to the bright shell (Figure 8), and perhaps some nuclear emission is not ruled out in this object (M. Hayes 2019, private communication).

Intriguingly, Berg et al. (2019a) recently reported observations of resonantly scattered C IV line profiles in two local starbursts having very strong C IV $\lambda\lambda1548,1550$ emission and He II $\lambda1640$ emission. Such resonant scattering implies large column densities of this relatively hot, highly ionized gas, with optical depths of $\tau_{C\,IV} \sim 10,000$. Since our models show that C IV is especially prevalent in outflows with strong cooling, rather than conventional, adiabatic superbubble feedback (Figure 7), could these observations indicate catastrophic cooling? For a C IV scattering cross section of $3 \times 10^{-14}\,cm^2$ at $\sim10^5$ K (e.g., Sankrit & Wood 2001), the implied value of $\tau_{C\,IV}$ requires a C IV density of $n_{C\,IV} \sim 10^{-2}$ in a 10 pc column. For C/H abundance on the order of 10^{-4}, this implies electron densities of $n_e \sim 100-1000\,cm^{-3}$, depending on the ionic fraction of C IV. However, C IV does not dominate in the higher-density regions. In our models, high densities are only found at the hot center near the ionizing SSC, and in the cooler shell; the C IV abundance is low in both of these regions (Figure 9).

Indeed, high $n_{C\,IV}$ is extremely difficult to maintain because of the efficiency of the cooling functions at temperatures where C IV dominates (e.g., Figure 2), explaining the lack of resonantly scattered C IV observations in diffuse gas. The $\tau_{C\,IV}$ in our catastrophic cooling models are still generally 2–3 orders of magnitude too small to cause significant resonant scattering. Thus, given the difficulty of generating high enough $n_{C\,IV}$ in starbursts, it may be more likely that the Berg et al. (2019a) observations do not show resonant scattering, and instead show more conventional, kinematic effects. The line splitting and broader profiles may be due to, e.g., hot, turbulent, bipolar flows. Berg et al. (2019a) compare the C IV emission-line profiles to those for O III], which exists at $10\times$ lower temperatures and is not strongly co-spatial with C IV. On the other hand, there may be extreme catastrophic cooling conditions where $\tau_{C\,IV}$ is high enough to generate resonant scattering. Further study of a wider parameter space is needed to evaluate this possibility.

If catastrophic cooling is present in extreme, compact starbursts, then the emission-line spectra will not reflect pure photoionization, as is ordinarily assumed when interpreting such spectra. In particular, the outflow kinematics generate higher ionization states that elevate emission in the corresponding species, as already suggested by, e.g., Gray & Scannapieco (2017). Thus, it may not be necessary to invoke hotter or composite photoionizing sources in extreme starbursts, as is often suggested to be necessary (e.g., Jaskot & Oey 2013; Senchyna et al. 2017; Nakajima et al. 2018; Berg et al. 2019a). Density-bounded conditions also can drastically affect the line ratios, as seen for the integrated line emission of model ETA006N1 in Table 4.

6. Summary and Conclusion

We have presented here a set of one-dimensional models that aim to study a range of radiative cooling regimes within SSC outflows. Our models track the non-equilibrium evolution of several atomic species and compute the cooling from these species on an ion-by-ion basis. The outflow is based on the

classic outflow model presented by Chevalier & Clegg (1985) and Weaver et al. (1977), and is defined by the mass-input rate ($\dot{M}$), the mechanical luminosity (L_{mech}), the injection (sonic) radius (R_{inj}), the ambient density (n_{amb}), and ambient temperature (T_{amb}). Our model defines the energy input rate as a function of the injection velocity. The outflow model is defined as a boundary condition at R_{inj} of each model, with initial ionization states set to their CIE values.

We present results from four models with the $\dot{M} = 10^{-2}\ M_{\odot}\,\mathrm{yr}^{-1}$, an injection (sonic) radius of $R_{inj} = 5\,\mathrm{pc}$, an ambient density of $n_{amb} = 500\,\mathrm{cm}^{-3}$, and varying the heating efficiency between 1 and 0.06, parameterized by an injection velocity between 1000 and $250\,\mathrm{km\,s}^{-1}$. With these initial conditions the outflow densities vary by a factor of 4, while the outflow temperature varies by a factor of 16. This range of energy injection rates generates a wide range of outflow structures. The classic adiabatic solution corresponds to model ETA100, which has the fastest outflow velocity. This model reproduces the three primary outflow features, the free-wind region, the shocked-wind region, and the swept-up shell and forward shock. For models with slower outflow velocities, ETA025 and ETA006, the shocked-wind region fails to form, and for the latter, the free-wind region itself is strongly cooling and non-adiabatic. In these models, it is the properties of the outflow that cause suppressed superwinds by catastrophic cooling, and not the physical conditions of the surrounding ambient medium.

The line emission from these outflows is computed by post-processing the density and temperature profiles from MAIHEM using the microphysics code CLOUDY (Ferland et al. 2013). Two sets of CLOUDY models are run: one where CLOUDY computes the ionization states assuming that the ionization states are in CIE, and one where the non-equilibrium ionization states are taken from MAIHEM. We find that for the cooling, non-adiabatic conditions, the non-equilibrium atomic models tend to produce more highly ionized conditions compared to the equilibrium models. This is true for nearly every element that is tracked by our atomics package. Therefore, we find that the non-equilibrium models tend to predict lower emissivities compared to the equilibrium models, for the nebular emission lines computed here.

Again using CLOUDY, we have studied the effect of a photoionizing background on the line emission, using a SB99 ionizing SED appropriate for a SSC responsible for generating the modeled outflow. Four models were considered: a control where no background UV field was applied, but using the density and temperature profiles from MAIHEM; one that considers pure photoionization on the same density profile, but assuming the gas is neutral, such that the temperature of the outflow is determined by photoheating only; one with density and temperature profiles from MAIHEM plus photoionization from the SB99 spectrum; and one with a MAIHEM model expanding into a lower-density, $1\,\mathrm{cm}^{-3}$ ambient medium at 10^4 K. The ambient density strongly affects the radial profile for the modeled emission. In high-density models, the collisional line emission is limited to the outer regions of the free-wind zone, and increases with radius; whereas in the low-density model, most collisional species decrease with radius except for a gap in the innermost region.

The inclusion of a background UV field has little effect on high-ionization species generated by gas temperatures of 10^6–10^7 K. However, photoionization has a dramatic impact on some emission lines originating from a strongly cooling flow. C IV $\lambda1549,1551$ and O VI $\lambda1037$, for example, show an increase in emission of roughly two orders of magnitude with photoionization, compared to without. In contrast, low-ionization species like [O II[$\lambda3727$ are basically eliminated from the free-wind zone. Moreover, in an optically thin, density-bounded shell, He II $\lambda1640$ and $\lambda4686$ are also strongly enhanced above photoionized values.

Our models suggest that C IV and O VI may serve as diagnostics of catastrophic cooling conditions. Observations show that when seen as nebular line emission, these transitions are associated with extreme starbursts where catastrophic cooling is likely to occur. These include objects like extreme Green Peas, which are often found to be optically thin to LyC radiation. He II, C III], Si IV, and Si III may also be useful, especially where photoionization is density-bounded. Further study is needed to fully understand their emission.

Other evidence for suppressed superwinds and strong clumping in objects like extreme Green Peas is consistent with the presence of catastrophically cooling outflows, and the resulting picket fence geometry can explain the escape of LyC radiation from these systems (Jaskot et al. 2019). Although our 1D models are not capable of simulating this clumping, the results presented here provide some initial insight on line emission from catastrophically cooling outflows, highlighting the importance of non-equilibrium atomic chemistry and predicted line diagnostics.

Understanding the expected line emissivities in these conditions can clarify the nature of Green Peas and their mechanism for LyC escape, as well as other starbursts experiencing these strongly cooling outflows. Future studies will expand on the simulation conditions and study a wider parameter space that includes varying the mass-input rate in order to gain a better understanding of when catastrophic cooling occurs and the range of predicted line emission. Hydrodynamical effects, such as instability-induced gas clumping will also be studied by expanding these simulations into two dimensions.

Appendix A
Normalized Emission-line Plots

Figures 10–13 show the line emission results relative to Hβ as a function of radius. The captions give the name of the original figure.
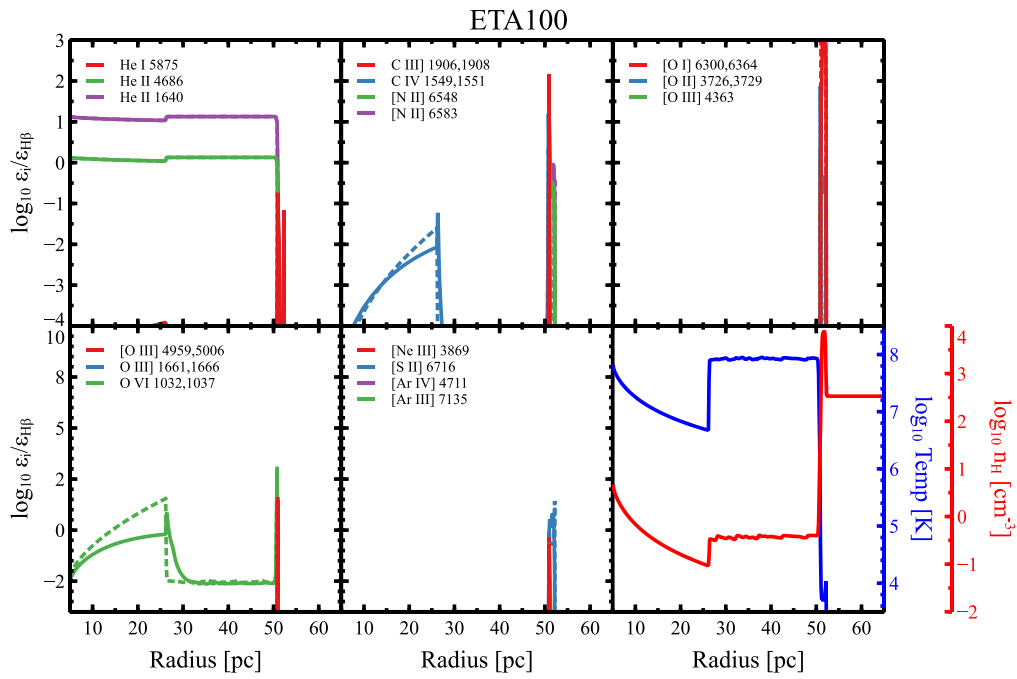
Figure 10. Line emission results for ETA100. This figure is the same as Figure 4 except now each line is normalized by Hβ. The solid lines represent emissivity ratios computed using the non-CIE, MAIHEM ionization states and the dotted line shows the equilibrium CLOUDY results.
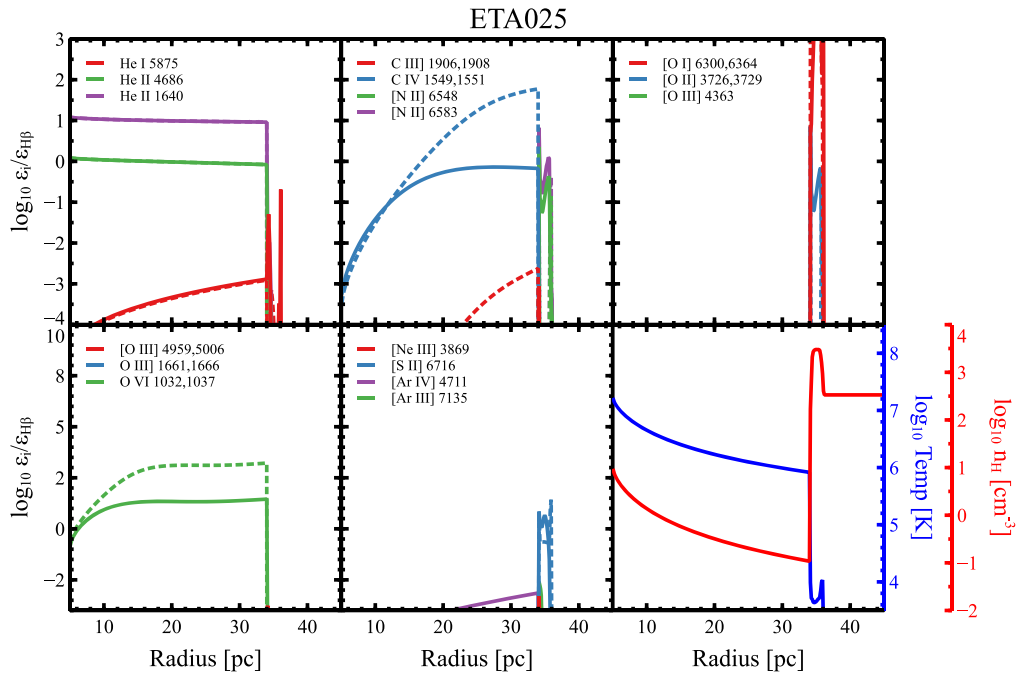

Figure 11. Line emission results for ETA025. This figure is the same as Figure 5 except now each line is normalized by Hβ.
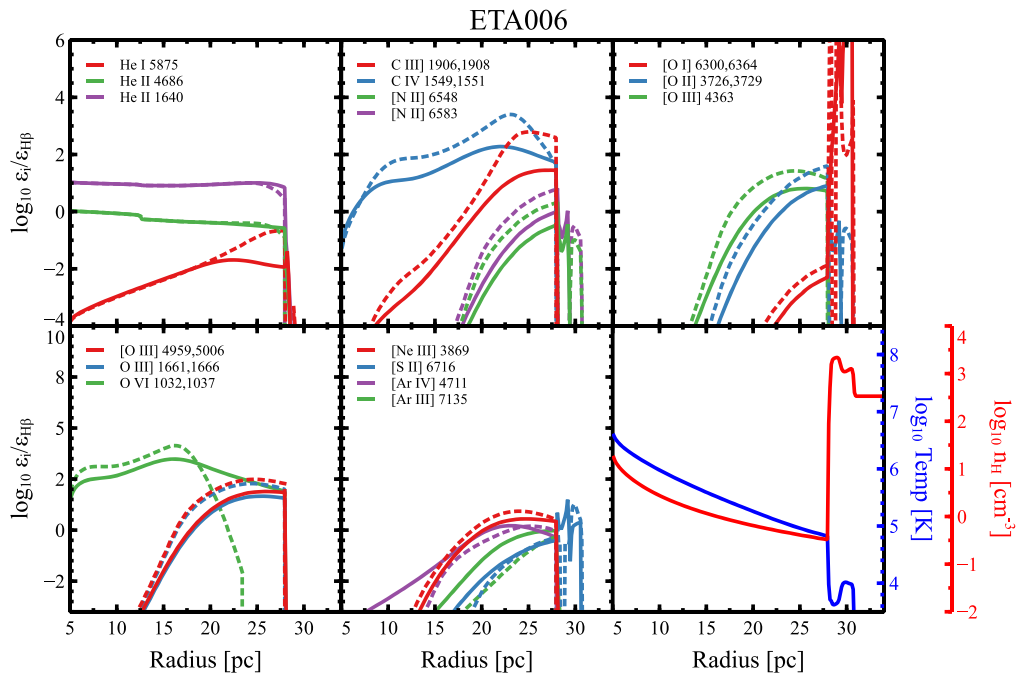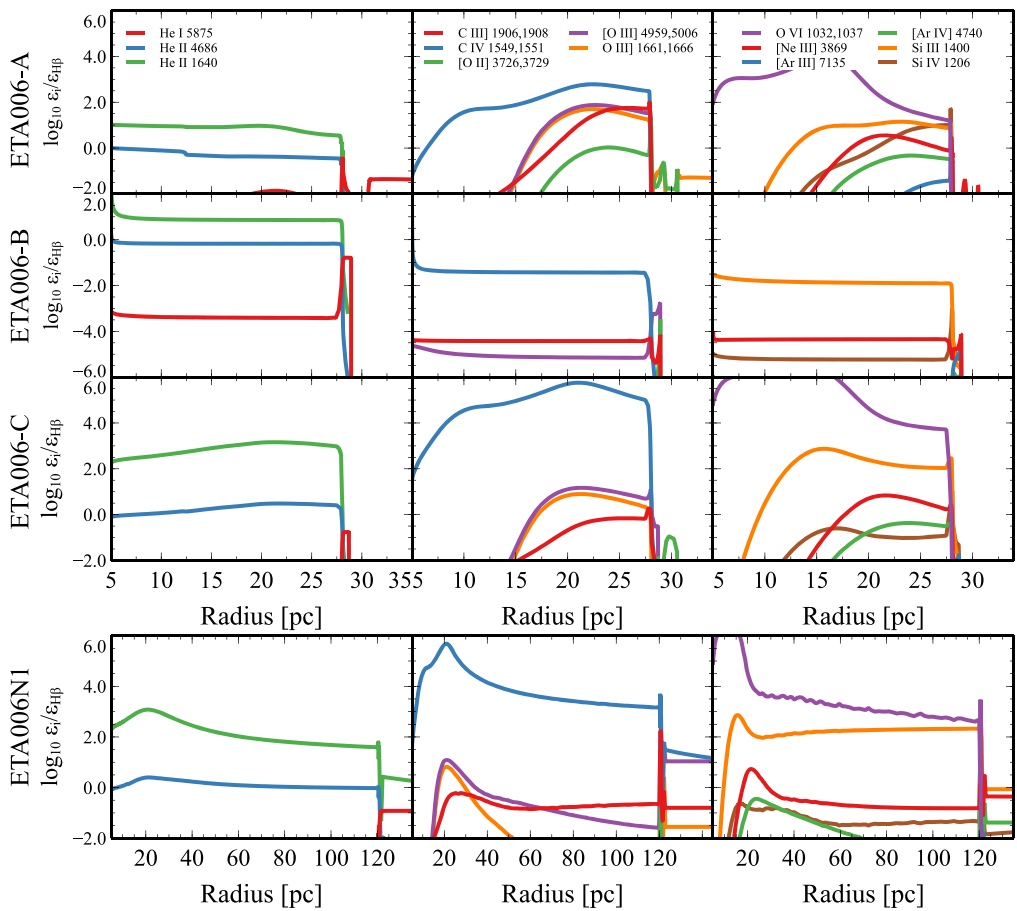
Figure 12. Line emission results for ETA006. This figure is the same as Figure 6 except now each line is normalized by Hβ.

Figure 13. Results for ETA006 with photoionization. This figure is the same as Figure 8 except now each line is normalized by Hβ.

Appendix B
SSC Photoionization of Wind-driven Shells

Wind-driven shells may be partially or completely ionized by the SSC LyC. The gas density in the ionized part of the shell is

$$\rho_{\mathrm{H\,II}} = \mu_i P_w / k T_{\mathrm{H\,II}} \qquad (12)$$

where $\mu_i = 14/23\, m_{\mathrm{H}}$ is the mean mass per particle in the completely ionized gas with 1 helium atom per each 10 hydrogen atoms, m_{H} is the mass of the hydrogen atom, P_w is the gas pressure in the shocked (model ETA100) or free (models ETA025 and ETA006) wind regions at the inner edge of the shell, k is the Boltzmann constant, and $T_{\mathrm{H\,II}} = 10^4$ K is the ionized gas temperature. The ion number density then is

$$n_i = \rho_{\mathrm{H\,II}} / \mu_a = \mu_i P_w / k \mu_a T_{\mathrm{H\,II}} \qquad (13)$$

where $\mu_a = 14/11\, m_{\mathrm{H}}$ is the mean mass per ion. The outer radius of the ionized zone $R_{\mathrm{H\,II}}$ is determined by the equation

$$Q = \frac{4\pi}{3} \beta n_i^2 (R_{\mathrm{H\,II}}^3 - R_{\mathrm{in}}^3) \qquad (14)$$

where Q is the number of the LyC photons emitted by the star cluster per unit time, R_{in} is the shell inner radius and $\beta = 2.59 \times 10^{-13}\,\mathrm{cm}^3\,\mathrm{s}^{-1}$ is the hydrogen recombination coefficient to all but the ground level.

The Starburst99 model and R_{in} determine the value of Q for our different models (see Figure 3). Equations (12) and (14) allow one to determine the ionized gas mass:

$$M_{\mathrm{H\,II}} = \frac{4\pi}{3} (R_{\mathrm{H\,II}}^3 - R_{\mathrm{in}}^3) \rho_{\mathrm{H\,II}} = \frac{k Q T_{\mathrm{H\,II}} \mu_a^2}{\beta \mu_i P_w}. \qquad (15)$$

One can compare this with the wind-driven shell mass

$$M_{\mathrm{sh}} = \frac{4\pi}{3} R_{\mathrm{sh}}^3 \rho_{\mathrm{amb}} \qquad (16)$$

where R_{sh} is the leading shock radius (see Figure 3) and ρ_{amb} is the ambient gas density (see Table 1). Note that in model ETA100 $P_w \sim P_{\mathrm{th}}$, where P_{th} is the gas thermal pressure in the shocked-wind zone, whereas in models ETA025 and ETA006 $P_w \sim P_{\mathrm{ram}}$, where $P_{\mathrm{ram}} = \rho_w V_w^2$ is the star cluster wind ram pressure at the inner edge of the shell. ρ_w and $V_w \sim 2 \times v_{\mathrm{inj}}$ are the star cluster wind density at the inner edge of the shell and the star cluster wind terminal speed, respectively.

ORCID iDs

M. S. Oey ⓘ https://orcid.org/0000-0002-5808-1320
Sergiy Silich ⓘ https://orcid.org/0000-0002-3814-5294
Evan Scannapieco ⓘ https://orcid.org/0000-0002-3193-1196

References

Agertz, O., & Kravtsov, A. V. 2015, ApJ, 804, 18
Amorín, R., Fontana, A., Pérez-Montero, E., et al. 2017, NatAs, 1, 0052
Amorín, R., Pérez-Montero, E., Vílchez, J. M., & Papaderos, P. 2012, ApJ, 749, 185
Badnell, N. R. 2006, ApJS, 167, 334
Badnell, N. R., O'Mullane, M. G., Summers, H. P., et al. 2003, A&A, 406, 1151
Benson, A. J., Bower, R. G., Frenk, C. S., et al. 2003, ApJ, 599, 38
Berg, D. A., Chisholm, J., Erb, D. K., et al. 2019a, ApJL, 878, L3
Berg, D. A., Erb, D. K., Henry, R. B. C., Skillman, E. D., & McQuinn, K. B. W. 2019b, ApJ, 874, 93
Bieri, R., Dubois, Y., Silk, J., Mamon, G. A., & Gaibler, V. 2016, MNRAS, 455, 4166
Bik, A., Östlin, G., Menacho, V., et al. 2018, A&A, 619, A131
Bolatto, A. D., Warren, S. R., Leroy, A. K., et al. 2013, Natur, 499, 450
Bordoloi, R., Lilly, S. J., Hardmeier, E., et al. 2014, ApJ, 794, 130
Bordoloi, R., Rigby, J. R., Tumlinson, J., et al. 2016, MNRAS, 458, 1891
Bouwens, R. J., Illingworth, G. D., Oesch, P. A., et al. 2012, ApJL, 752, L5
Bustard, C., Zweibel, E. G., & D'Onghia, E. 2016, ApJ, 819, 29
Cantó, J., Raga, A. C., & Rodríguez, L. F. 2000, ApJ, 536, 896
Cardamone, C., Schawinski, K., Sarzi, M., et al. 2009, MNRAS, 399, 1191
Chevalier, R. A., & Clegg, A. W. 1985, Natur, 317, 44
Chisholm, J., Tremonti, C. A., Leitherer, C., Chen, Y., & Wofford, A. 2016, MNRAS, 457, 3133
Cohen, D. P., Turner, J. L., Consiglio, S. M., Martin, E. C., & Beck, S. C. 2018, ApJ, 860, 47
Cole, S., Lacey, C. G., Baugh, C. M., & Frenk, C. S. 2000, MNRAS, 319, 168
Creasey, P., Theuns, T., & Bower, R. G. 2013, MNRAS, 429, 1922
Dalla Vecchia, C., & Schaye, J. 2008, MNRAS, 387, 1431
Davé, R., Finlator, K., & Oppenheimer, B. D. 2011, MNRAS, 416, 1354
Dove, J. B., Shull, J. M., & Ferrara, A. 2000, ApJ, 531, 846
Edgar, R. J., & Chevalier, R. A. 1986, ApJL, 310, L27
Farber, R., Ruszkowski, M., Yang, H. Y. K., & Zweibel, E. G. 2018, ApJ, 856, 112
Faucher-Giguère, C.-A., Lidz, A., Zaldarriaga, M., & Hernquist, L. 2009, ApJ, 703, 1416
Ferland, G. J., Porter, R. L., van Hoof, P. A. M., et al. 2013, RMxAA, 49, 137
Fragile, P. C., Anninos, P., Croft, S., Lacy, M., & Witry, J. W. L. 2017, ApJ, 850, 171
Fryxell, B., Olson, K., Ricker, P., et al. 2000, ApJS, 131, 273
Gnat, O. 2017, ApJS, 228, 11
Gnat, O., & Ferland, G. J. 2012, ApJS, 199, 20
Gnat, O., & Sternberg, A. 2007, ApJS, 168, 213
Gray, W. J., & Scannapieco, E. 2010, ApJ, 718, 417
Gray, W. J., & Scannapieco, E. 2011a, ApJ, 733, 88
Gray, W. J., & Scannapieco, E. 2011b, ApJ, 742, 100
Gray, W. J., & Scannapieco, E. 2016, ApJ, 818, 198
Gray, W. J., & Scannapieco, E. 2017, ApJ, 849, 132
Gray, W. J., Scannapieco, E., & Kasen, D. 2015, ApJ, 801, 107
Gray, W. J., Scannapieco, E., & Lehnert, M. D. 2019, ApJ, 875, 110
Gupta, S., Nath, B. B., Sharma, P., & Shchekinov, Y. 2016, MNRAS, 462, 4532
Hayes, M., Melinder, J., Östlin, G., et al. 2016, ApJ, 828, 49
Hayward, C. C., & Hopkins, P. F. 2017, MNRAS, 465, 1682
Heckman, T. M., Alexandroff, R. M., Borthakur, S., Overzier, R., & Leitherer, C. 2015, ApJ, 809, 147
Heckman, T. M., Armus, L., & Miley, G. K. 1990, ApJS, 74, 833
Heckman, T. M., Borthakur, S., Overzier, R., et al. 2011, ApJ, 730, 5
Heckman, T. M., Lehnert, M. D., Strickland, D. K., & Armus, L. 2000, ApJS, 129, 493
Henley, D. B., Kwak, K., & Shelton, R. L. 2012, ApJ, 753, 58
Hopkins, P. F., Quataert, E., & Murray, N. 2011, MNRAS, 417, 950
Hopkins, P. F., Quataert, E., & Murray, N. 2012, MNRAS, 421, 3522
Izotov, Y. I., Guseva, N. G., & Thuan, T. X. 2011, ApJ, 728, 161
Jaskot, A. E., Dowd, T., Oey, M. S., Scarlata, C., & McKinney, J. 2019, ApJ, 885, 96
Jaskot, A. E., & Oey, M. S. 2013, ApJ, 766, 91
Jaskot, A. E., Oey, M. S., Scarlata, C., & Dowd, T. 2017, ApJL, 851, L9
Krause, M. G. H., & Diehl, R. 2014, ApJL, 794, L21
Krumholz, M. R., & Matzner, C. D. 2009, ApJ, 703, 1352
Kwak, K., & Shelton, R. L. 2010, ApJ, 719, 523
Lehnert, M. D., & Heckman, T. M. 1996, ApJ, 462, 651
Lehnert, M. D., Heckman, T. M., & Weaver, K. A. 1999, ApJ, 523, 575
Lehnert, M. D., Nesvadba, N. P. H., Cuby, J.-G., et al. 2010, Natur, 467, 940
Leitherer, C., Schaerer, D., Goldader, J. D., et al. 1999, ApJS, 123, 3
Leroy, A. K., Bolatto, A. D., Ostriker, E. C., et al. 2018, ApJ, 869, 126
Lu, Y., Blanc, G. A., & Benson, A. 2015, ApJ, 808, 129
Mac Low, M.-M., & Ferrara, A. 1999, ApJ, 513, 142
Martin, C. L. 1999, ApJ, 513, 156
Martin, C. L. 2005, ApJ, 621, 227
Martin, C. L., Dijkstra, M., Henry, A., et al. 2015, ApJ, 803, 6
Martin, C. L., Shapley, A. E., Coil, A. L., et al. 2012, ApJ, 760, 127
Martínez-González, S., Silich, S., & Tenorio-Tagle, G. 2014, ApJ, 785, 164
McKinney, J. H., Jaskot, A. E., Oey, M. S., et al. 2019, ApJ, 874, 52
Mori, M., Ferrara, A., & Madau, P. 2002, ApJ, 571, 40

Mukherjee, D., Bicknell, G. V., Wagner, A. Y., Sutherland, R. S., & Silk, J. 2018, MNRAS, 479, 5544

Muratov, A. L., Kereš, D., Faucher- Giguère, C.-A., et al. 2015, MNRAS, 454, 2691

Murray, N., Ménard, B., & Thompson, T. A. 2011, ApJ, 735, 66

Nakajima, K., Schaerer, D., Le Fèvre, O., et al. 2018, A&A, 612, A94

Oey, M. S., Herrera, C. N., Silich, S., et al. 2017, ApJL, 849, L1

Oppenheimer, B. D., Davé, R., & Finlator, K. 2009, MNRAS, 396, 729

Pellegrini, E., Drory, N., Lopez, L. A., et al. 2019, BAAS, 51, 406

Pettini, M., Rix, S. A., Steidel, C. C., et al. 2002, ApJ, 569, 742

Pettini, M., Shapley, A. E., Steidel, C. C., et al. 2001, ApJ, 554, 981

Rahner, D., Pellegrini, E. W., Glover, S. C. O., & Klessen, R. S. 2017, MNRAS, 470, 4453

Rayleigh, L. 1883, Proc. Lond. Math. Soc., 14, 170

Rivera-Thorsen, T. E., Östlin, G., Hayes, M., & Puschnig, J. 2017, ApJ, 837, 29

Rubin, K. H. R., Prochaska, J. X., Koo, D. C., et al. 2014, ApJ, 794, 156

Rupke, D. S., Veilleux, S., & Sanders, D. B. 2005, ApJS, 160, 115

Sankrit, R., & Wood, K. 2001, ApJ, 555, 532

Scannapieco, E. 2017, ApJ, 837, 28

Scannapieco, E., Ferrara, A., & Madau, P. 2002, ApJ, 574, 590

Scannapieco, E., Thacker, R. J., & Davis, M. 2001, ApJ, 557, 605

Scannapieco, E., Weisheit, J., & Harlow, F. 2004, ApJ, 615, 29

Schneider, E. E., Robertson, B. E., & Thompson, T. A. 2018, ApJ, 862, 56

Senchyna, P., Stark, D. P., Vidal-García, A., et al. 2017, MNRAS, 472, 2608

Shapiro, P. R., & Benjamin, R. A. 1991, PASP, 103, 923

Shelton, R. L., & Kwak, K. 2018, ApJ, 866, 34

Shull, J. M. 1979, ApJ, 234, 761

Silich, S., & Tenorio-Tagle, G. 2017, MNRAS, 465, 1375

Silich, S., & Tenorio-Tagle, G. 2018, MNRAS, 478, 5112

Silich, S., Tenorio-Tagle, G., & Muñoz- Tuñón, C. 2007, ApJ, 669, 952

Silich, S., Tenorio-Tagle, G., & Rodríguez- González, A. 2004, ApJ, 610, 226

Silich, S., Tenorio-Tagle, G., Torres-Campos, A., et al. 2009, ApJ, 700, 931

Smith, L. J., Westmoquette, M. S., Gallagher, J. S., et al. 2006, MNRAS, 370, 513

Socrates, A., Davis, S. W., & Ramirez-Ruiz, E. 2008, ApJ, 687, 202

Somerville, R. S., & Primack, J. R. 1999, MNRAS, 310, 1087

Soto, K. T., Martin, C. L., Prescott, M. K. M., & Armus, L. 2012, ApJ, 757, 86

Springel, V., & Hernquist, L. 2003, MNRAS, 339, 289

Stevens, I. R., & Hartwell, J. M. 2003, MNRAS, 339, 280

Strickland, D. K., & Heckman, T. M. 2007, ApJ, 658, 258

Strickland, D. K., & Heckman, T. M. 2009, ApJ, 697, 2030

Sturm, E., González-Alfonso, E., Veilleux, S., et al. 2011, ApJL, 733, L16

Sur, S., Scannapieco, E., & Ostriker, E. C. 2016, ApJ, 818, 28

Sutherland, R. S., & Dopita, M. A. 1993, ApJS, 88, 253

Taylor, G. 1950, RSPSA, 201, 192

Thompson, T. A., Fabian, A. C., Quataert, E., & Murray, N. 2015, MNRAS, 449, 147

Thompson, T. A., Quataert, E., & Murray, N. 2005, ApJ, 630, 167

Thompson, T. A., Quataert, E., Zhang, D., & Weinberg, D. H. 2016, MNRAS, 455, 1830

Tremonti, C. A., Heckman, T. M., Kauffmann, G., et al. 2004, ApJ, 613, 898

Tremonti, C. A., Moustakas, J., & Diamond-Stanic, A. M. 2007, ApJL, 663, L77

Turk, M. J., Smith, B. D., Oishi, J. S., et al. 2011, ApJS, 192, 9

Turner, J. L., Beck, S. C., Crosthwaite, L. P., et al. 2003, Natur, 423, 621

Turner, J. L., Consiglio, S. M., Beck, S. C., et al. 2017, ApJ, 846, 73

Uhlig, M., Pfrommer, C., Sharma, M., et al. 2012, MNRAS, 423, 2374

Vasiliev, E. O. 2011, MNRAS, 414, 3145

Veilleux, S., Cecil, G., & Bland-Hawthorn, J. 2005, ARA&A, 43, 769

Voronov, G. S. 1997, ADNDT, 65, 1

Walter, F., Weiss, A., & Scoville, N. 2002, ApJL, 580, L21

Wang, B. 1995a, ApJ, 444, 590

Wang, B. 1995b, ApJL, 444, L17

Weaver, R., McCray, R., Castor, J., Shapiro, P., & Moore, R. 1977, ApJ, 218, 377

Weiner, B. J., Coil, A. L., Prochaska, J. X., et al. 2009, ApJ, 692, 187

Wünsch, R., Silich, S., Palouš, J., Tenorio-Tagle, G., & Muñoz-Tuñón, C. 2011, ApJ, 740, 75

Yadav, N., Mukherjee, D., Sharma, P., & Nath, B. B. 2017, MNRAS, 465, 1720

Zastrow, J., Oey, M. S., Veilleux, S., & McDonald, M. 2013, ApJ, 779, 76

Zhang, D. 2018, Galax, 6, 114